Intermolecular interactions in antipyrine-like derivatives 2-halo-*N*-(1,5-dimethyl-3-oxo-2-phenyl-2,3-dihydro-1-*H*-pyrazol-4-yl)benzamides: X-ray structure, Hirshfeld surface analysis and DFT calculations

Aamer Saeed,[a*] Asma Khurshid,[a] Ulrich Flörke,[b] Gustavo A. Echeverría,[c] Oscar E. Piro,[c] Diego M. Gil,[d,*] Mariana Rocha,[e] Antonio Frontera,[f] Hesham R. El-Seedi,[g,h] Amara Mumtaz,[i] Mauricio F. Erben[j*]

[a] Department of Chemistry, Quaid-I-Azam University, 45320, Islamabad, Pakistan.

[b] Department Chemie, Fakultät für Naturwissenschaften, Universität Paderborn, Warburgerstrasse 100, D-33098 Paderborn, Germany

[c] Departamento de Física, Facultad de Ciencias Exactas, Universidad Nacional de La Plata e Instituto de Física La Plata, IFLP (UNLP, CONICET, CCT-La Plata), C. C. 67, 1900 La Plata, Argentina.

[d] INBIOFAL (CONICET-UNT). Instituto de Química Orgánica. Facultad de Bioquímica, Química y Farmacia. Universidad Nacional de Tucumán. Ayacucho 471. T4000INI. San Miguel de Tucumán. Argentina.

[e] INBIOFAL (CONICET-UNT). Cátedra de Física. Facultad de Agronomía y Zootecnia. Universidad Nacional de Tucumán. Av. Néstor Kirchner 1900. 4000. San Miguel de Tucumán. Argentina.

[f] Departament de Química, Universitat de les Illes Balears, Crta de Valldemossa km 7.5, 07122 Palma de Mallorca (Baleares), Spain.

[g] College of Food and Biological Engineering, Jiangsu University, Zhenjiang 212013, China

[h] Al-Rayan Colleges, Medina 42541, Saudi Arabia.

[i] Department of Chemistry, COMSATS University Islamabad, Abbottabad Campus, Abbottabad 22060, Pakistan.

[j] CEQUINOR (UNLP-CONICET, CCT-La Plata), Departamento de Química, Facultad de Ciencias Exactas, Universidad Nacional de La Plata, Boulevard 120 e/ 60 y 64 Nº1465 La Plata B1900, Buenos Aires, Argentina.

* Corresponding authors: aamersaeed@yahoo.com (A.S.), diego.gil@fbqf.unt.edu.ar (D.M.G.), erben@quimica.unlp.edu.ar (M.F.E.).

Abstract

The synthesis, structural X-ray characterization, Hirshfeld surface analysis and DFT calculations of two new antipyrine derivatives are reported herein. Particularly, 2-bromo-N-(2,3-dihydro-1,5-dimethyl-3-oxo-2-phenyl-*1H*-pyrazol-4-yl)benzamide (**1**) and 2-chloro-N-(2,3-dihydro-1,5-dimethyl-3-oxo-2-phenyl-*1H*-pyrazol-4-yl)benzamide (**2**) are synthesized in good yields and characterized spectroscopically. Both compounds are isostructural and crystallize in the monoclinic $P2_1/c$ space group. The crystal packing of both compounds is mainly stabilized by a combination of N-H···O and C-H···O hydrogen bonds. In addition, C-H···π and lone pair···π contacts were observed. Their solid-state structures have been analyzed through Hirshfeld surface analysis, including the evaluation of the different energy frameworks, indicating that the molecular sheets are primarily formed by hydrogen bonds and the stabilization is dominated via the electrostatic energy contribution. These studies are complemented with DFT calculations (B3LYP-D3/def2-TZVP), and a combination of QTAIM/NCIplot analyses disclosing that the H-bonding interactions are energetically relevant (ranging from 0.9 to 6.1 kcal/mol), however the total binding energies of the different assemblies are dominated by a combination of π-interactions (of the type C-H···π, π···π, and lone pair halogen···π) that are able to stabilize cooperatively the assemblies up to 12 kcal/mol.

Keywords: Antipyrine derivatives; X-ray structure; Non-covalent interactions; Hirshfeld surfaces; Energy frameworks

1. Introduction

Interest in antipyrine derivatives (APDs) can be traced back to the synthesis of the first of such derivatives, namely aminophenazone, by Knorr in 1833 and have been the subject matter of research in a variety of fields **[1].** Aminophenazone derivatives have been shown to possess pharmacological applications as antipyretic **[2]**, analgesic **[3]**, and anti-inflammatory agents **[4, 5].** The presence of amide linkage confers to aminophenazone moiety useful biological activities. Since amides are an important class of organic compounds, they are synthesized in a number of ways, including either direct coupling of carboxylic acids and amines at high temperatures or through microwave-assisted methodologies and by means of organo-catalysts. The exploration of amidic linkage in various drugs has disclosed the importance of amides and broadened the scope of their pharmacological applications as anthelmintic **[6]**, antihistamine **[7]**, antifungal **[8]**, and antibacterial **[9, 10]**. Hybrid compounds containing the antipyrine and thiazolyl or thiadiazolyl groups have been tailored to act as potential non-acidic anti-inflammatory agents [**11**].

Crystal engineering and supramolecular interactions, including non-covalent interactions, have attracted considerable attention in the design of new receptors and supramolecular materials **[12-15]**. Non-covalent interactions such as hydrogen bonding, halogen bonding, C-H···π interactions, π-π stacking, dispersive interactions, σ-hole interactions, π-hole interactions, and other weak contacts play crucial roles in various fields of medicinal chemistry and materials science **[16-20]**. It is well-known that the crystal packing is the result of the synergistic contributions of different types of strong and weak non-covalent interactions and it is very important to study the cooperativity and competition of these non-covalent interactions. A proper understanding of these interactions is crucial to extrapolate structure-activity/property relationships.

We report here the synthesis and X-ray crystal structure of two new antipyrine derivatives, namely 2-bromo-N-(2,3-dihydro-1,5-dimethyl-3-oxo-2-phenyl-*1H*-pyrazol-4-

yl)benzamide (**1**) and 2-chloro-N-(2,3-dihydro-1,5-dimethyl-3-oxo-2-phenyl-*1H*-pyrazol-4-yl)benzamide (**2**). Hirshfeld surface analysis was used to determine quantitatively the intermolecular interactions controlling the crystal packing of both compounds. In addition, we have calculated the interaction energies, including energy frameworks. The concept of energy frameworks allows for a better understanding of the intermolecular interactions as it graphically represents the total interaction energies or its individual components as cylindrical tubes joining molecules. The radii of these cylinders are mainly related with the strength of the corresponding intermolecular contacts. These calculations are of crucial importance in the evaluation of the contributions to the total intermolecular energies in molecular pairs from different structural motifs.

2. Experimental

2.1. Synthesis. A calculated amount of substituted aromatic acids **1** (0.1 g, 0.5 mmol) was refluxed for 1-2 hours with thionyl chloride (0.03 mL, 0.5 mmol) to form the respective acid halides. This was accompanied by the evolution of volatile gases like sulphur dioxide and hydrogen chloride, respectively. A solution of 4-aminophenazone (0.1 g, 0.5 mmol) dissolved in pyridine (0.03 mL, 0.5 mmol) was added to the acid halide formed *in situ* and the reaction mixture was refluxed for 3 hours (Scheme I). On formation of the product, confirmed by thin layer chromatography (TLC), the reaction mixture was filtered and the solid product purified by recrystallization in aqueous ethanol. A tentative mechanism for the formation of the benzamide moieties through the reaction of 4-aminophenazone and acyl halides is depicted in the Scheme S1 (ESI).

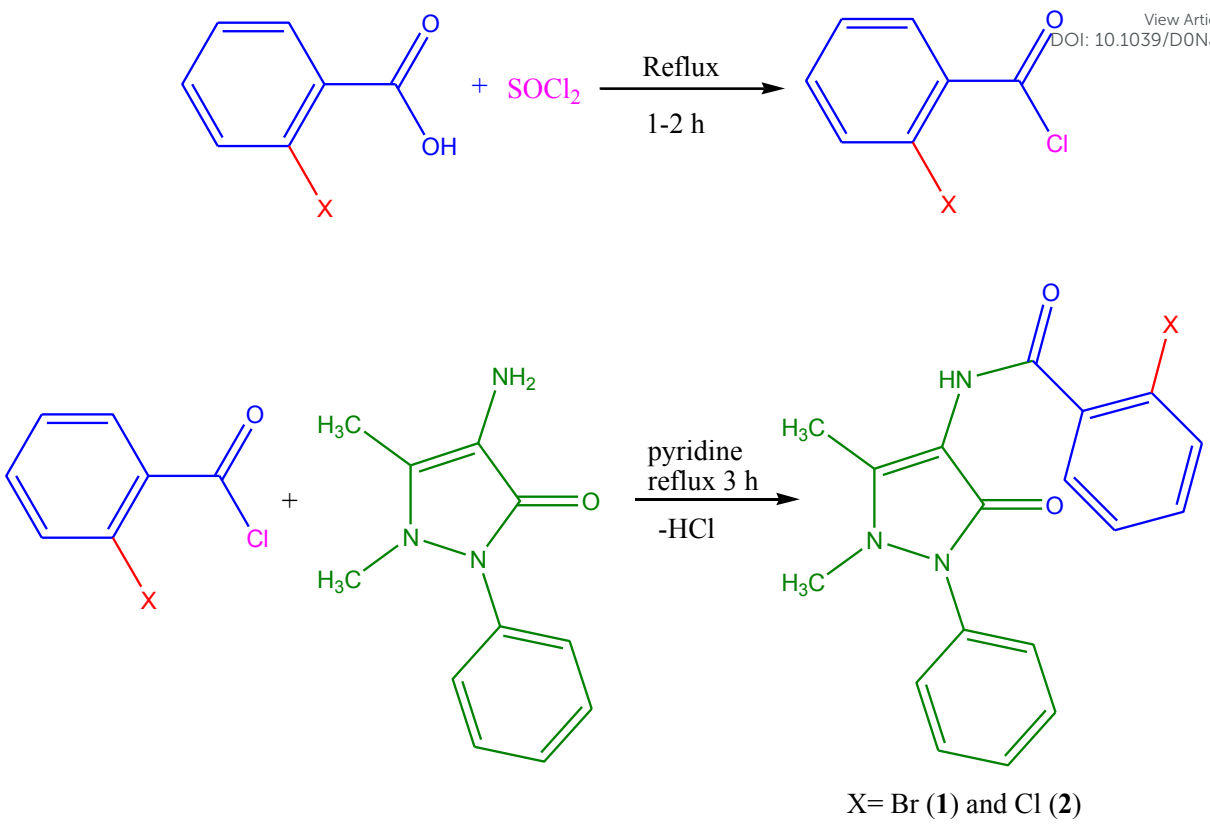

Scheme I. Synthesis of compounds **1** and **2**.

*2.1.1- 2-Bromo-N-(1,5-dimethyl-3-oxo-2-phenyl-2,3-dihydro-1H-pryazole-4-yl)benzamide (**1**):* Brown crystals, yield: 87%, m.p: 108-109 °C ; IR (KBr): 3151 (CO**NH**), 2990, 2832, (Csp^3-H), 1678 (**CO**NH), 1423, 1332 (Csp^3-H bending): ^{1}H-NMR ($CDCl_3$, 300MHz): δ 7.81 (s, 1H, N-H), 7.66-7.28 (m, 9H, Ar-H), 3.15 (s, 3H, C**H**$_3$-N-pyrazolone), 2.48 (s, 3H, C**H**$_3$-Csp^2-pyrazolone); ^{13}C-NMR ($CDCl_3$, 75MHz): δ 166.31 (**CO**NH), 161.19 (-C=C-**CO**-N-pyrazolone), 149.37 (C_6H_4Br-CO-**$C_{sp^2\text{-ipso}}$**), 137.29 (C_6H_5-**C_{sp^2}-ipso**), 134.37 (-**C**=C-pyrazolone), 133.46 (-C=**C**-pyrazolone), 131.56 (C_6H_4Br-**$C_{sp^2\text{-para}}$**), 129.63 (C_6H_4Br-**$C_{sp^2\text{-meta}}$**), 129.33 (C_6H_5-**$C_{sp^2\text{-meta}}$**), 127.56 (C_6H_5-**$C_{sp^2\text{-para}}$**), 124.40 (C_6H_5-**$C_{sp^2\text{-ortho}}$**), 36.09 (**CH**$_3$-N-pyrazolone), 12.81 (**CH**$_3$-C_{SP}^2- pyrazolone). GC-MS (m/z): 387 (M^+), 341, 321 (100%), 202, 119, 91. LC-MS (m/z) %: M^+386 (1:1), 368, 214, 203. Elemental analysis calculated for $C_{18}H_{16}BrN_3O_2$: C 59.42, H 4.09, N 9.21 %; found: C 59.47, H 4.06, N 9.19 %.

2.1.2- 2-Chloro-N-(1,5-dimethyl-3-oxo-2-phenyl-2,3-dihydro-1H-pryazole-4-yl)benzamide (2): Yellow crystalline solid; yield: 82%, m.p: 103-104 °C; IR (KBr): 3150 (CO**NH**), 2991, 2865, (Csp^3-H), 1675 (**CO**NH), 1435, 1346 (Csp^3-H bending): ^{1}H-NMR ($CDCl_3$, 300MHz): δ 7.64-7.60 (m, 3H, Ar-H), 7.45 (m, 2H, Ar-H), 7.40 (m, 3H, Ar-H), 7.37-7.26 (m, 2H, Ar-H, s, 1H, N-H), 3.13 (s, 3H, C**H**$_3$-N-pyrazolone), 2.41 (s, 3H, C**H**$_3$-Csp^2-pyrazolone); ^{13}C-NMR ($CDCl_3$, 75MHz): δ 166.25 (-**CO**NH), 161.36 (-C=C-**CO**-N- pyrazolone), 149.45 (C_6H_5-**C_{sp^2}-ipso**), 137.40 (C_6H_4Cl-CO-**C_{sp^2}-para**), 134.55 (C_6H_4Cl-CO-**C_{sp^2}-ipso**), 133.40 (-**C**=C-pyrazolone), 131.45 (-C=**C**-pyrazolone), 129.63 (C_6H_4Cl-**C_{sp^2}-ortho**), 129.24 (C_6H_5-**C_{sp^2}-meta**), 127.48 (C_6H_4Cl-**C_{sp^2}-ortho**), 126.98 (C_6H_4Cl-**C_{sp^2}-meta**), 124.21 (C_6H_4Cl-**C_{sp^2}-meta**), 119.70 (C_6H_5-**C_{sp^2}-para**), 108.31 (C_6H_5-**C_{sp^2}-ortho**), 36.17 (**CH$_3$**-N-), 12.79 (**CH$_3$**-C_{SP^2}-). LC-MS (m/z) %: 342 (M^+ with clear 3:1 $^{35/37}$Cl isotopic ratio), 214. Elemental analysis calculated for $C_{18}H_{16}ClN_3O_2$: C 61.21, H 6.78, N 14.40 %; found C 61.25, H 6.72, N 14.42 %.

2.2. Instrumentation. Melting points were determined with a Gallenkamp melting point apparatus (MP-D) and the values are uncorrected. Infrared absorption spectra of samples sandwiched between KBr pellets were recorded with a Shimadzu IR 460 spectrophotometer. ^{1}H-NMR spectra were obtained with a Bruker 300 NMR MHz spectrometer in $CDCl_3$ solution, using TMS as an internal reference. ^{13}CNMR spectra were obtained by (75 MHz) NMR spectrometer in $CDCl_3$ as solvent. Thin layer chromatography was performed on pre-coated silica gel aluminum plates (layer thickness 0.2 mm, HF 254, Reidal-de-Haen from Merck). Chromatogram was recorded using ultraviolet light (254 and 260 nm). Mass spectra were recorded on a LC/MSD InfinityLab LC Series 1260 from Agilent Technologies. Elemental analysis was performed on a LECO CHNS 932 instrument.

2.3. Crystal data and structure refinement. For **1**, X-ray diffraction intensities were collected on a Bruker SMART APEX CCD with graphite-monochromated MoKα (λ=0.71073 Å) radiation. Data were corrected semi-empirically for absorption from equivalent reflections. For

2, the measurements were performed on an Oxford Xcalibur Gemini, Eos CCD diffractometer with graphite-monochromated CuKα (λ=1.54178 Å) radiation. X-ray reflection intensities were collected (ω scans with ϑ and κ-offsets), integrated and scaled with CrysAlisPro **[21]** suite of programs. The unit cell parameters were obtained by least-squares refinement (based on the angular settings for all collected reflections with intensities larger than seven times the standard deviation of measurement errors) using CrysAlisPro. Data were corrected empirically for absorption employing the multi-scan method implemented in CrysAlisPro. Both structures were solved by direct methods with SHELXS of the SHELX suite of programs **[22]** and the molecular model refined with anisotropic displacement parameters for all non-H atoms by full-matrix least-squares procedure with SHELXL of the same package. For **1**, H-atom were located in difference Fourier maps and refined at idealized positions riding on the carbon or nitrogen atoms to which they are attached with isotropic displacement parameters $U_{iso}(H) = 1.2U_{eq}(C/N)$ or $1.5U_{eq}(CH_3)$ and C-H 0.95-0.98 Å and N-H 0.88 Å. For **2**, all hydrogen atoms were located among the first sixteen most intense peaks in a Fourier difference Fourier map phased on the heavier atoms and refined at their found positions with isotropic displacement parameters. Both CH_3 groups converged to staggered conformations.

Crystal data and structure refinement results are summarized in **Table 1**. Crystallographic structural data have been deposited at the Cambridge Crystallographic Data Centre (CCDC). Enquiries for data can be direct to: Cambridge Crystallographic Data Centre, 12 Union Road, Cambridge, UK, CB2 1EZ or (e-mail) deposit@ccdc.cam.ac.uk or (fax) +44 (0) 1223 336033. Any request to the Cambridge Crystallographic Data Centre for this material should quote the full literature citation and the reference number CCDC 1884126 (**1**) and 2008322 (**2**).

Table 1. Crystal data and structure refinement results for compounds (**1**) and (**2**).

Empirical formula	$C_{18}H_{16}BrN_3O_2$	$C_{18}H_{16}ClN_3O_2$

View Article Online
DOI: 10.1039/D0NJ03958F

Formula weight	386.25	341.79
Temperature	130(2) K	297(2) K
Wavelength	0.71073 Å	1.54184 Å
Crystal system	Monoclinic	Monoclinic
Space group	P $2_1/c$	P $2_1/c$
Unit cell dimensions	a = 14.1326(15) Å	a = 13.985(1) Å
	b = 6.1144(6) Å	b = 6.2373(4) Å
	c = 20.190(2) Å	c = 20.226(1) Å
	β = 106.033(2)°	β = 105.334(7)°
Volume	1676.6(3) $Å^3$	1701.5(2) $Å^3$
Z, density (calculated)	4, 1.530 Mg/m^3	4, 1.334 Mg/m^3
Absorption coefficient	2.467 mm^{-1}	2.115 mm^{-1}
F(000)	784	712
Crystal size	0.44 x 0.21 x 0.18 mm^3	0.184 x 0.157 x 0.040 mm^3
ϑ-range for data collection	1.50 to 27.88°	4.534 to 72.347°
Index ranges	$-18 \le h \le 18$	$-14 \le h \le 17$
	$-7 \le k \le 8$	$-7 \le k \le 3$
	$-26 \le l \le 24$	$-24 \le l \le 24$
Reflections collected	15171	6646
Independent reflections	3987 [R(int) = 0.027]	3303 [R(int) = 0.027]
Observed reflections [I>2σ(I)]	3323	2251
Completeness	100% to ϑ = 27.88°	99.9 % to ϑ = 67.684°
Refinement method	Full-matrix least-squares on F^2	
Data / restraints / parameters	3987 / 0 / 223	3303 / 0 / 281
Goodness-of-fit on F^2	1.062	1.010
Final R indices [I>2σ(I)]	R1 = 0.0334	R1 = 0.0489
	wR2 = 0.0837	wR2 = 0.1272
R indices (all data)	R1 = 0.0432	R1 = 0.0774
	wR2 = 0.0882	wR2 = 0.1518
Largest diff. peak and hole	0.638 and -0.257 e $Å^{-3}$	0.202 and -0.263 e $Å^{-3}$

$R_1=\Sigma||F_o|-|F_c||/\Sigma|F_o|$, $wR_2=[\Sigma w(|F_o|^2-|F_c|^2)^2/\Sigma w(|F_o|^2)^2]^{1/2}$. For **1** the largest diff. peak is 0.77 Å from Br1 position.

2.4. Hirshfeld surface calculations. Hirshfeld surfaces **[23]** and their associated two-dimensional fingerprint plots **[24]** can be considered as very convenient tools for the exploration of intermolecular interactions in numerous organic and inorganic compounds **[25]**. Different functions describe specific properties of the Hirshfeld surface (d_{norm}, shape index, or curvedness) allowing for intuitive recognition and visual analysis of interactions between

different molecules. In the case of d_{norm} surface, red spots are associated with contacts between atoms, which are shorter than the sum of van der Waals (vdW) radii, and for this reason are frequently used to visualize close contacts such as hydrogen bonds. The 2D fingerprint plots are used as a graphical summary of the contact distances to the Hirshfeld surface and allow us to decode and quantify the intermolecular contacts in the crystal lattice. Hirshfeld surfaces and 2D fingerprint plots were explored with the CrystalExplorer17.5 program **[26]** on crystal structures imported from CIF files.

2.5. Theoretical methods. The calculations of non-covalent interactions and molecular electrostatic potential (MEP) surfaces were carried out using Gaussian-16 **[27]** at the B3LYP-D3/def2-TZVP level of theory. The Grimme's D3 dispersion correction has been used in the calculations **[28]**. To evaluate the interactions in the solid state, the crystallographic coordinates were used and only the position of the H-bonds has been optimized. This procedure and level of theory has been successfully used to evaluate similar interactions in related systems **[29]**. The interaction energies were computed by calculating the difference between the energies of the isolated monomers and the ones of their assembly. The QTAIM analysis **[30]** and NCIplot index **[31]** have been computed at the same level of theory by means of the AIMAll program **[32]**.

3. Results and discussion

3.1. Description of crystal structures of compounds 1-2.

Figures 1a and **2a** show an ORTEP **[33]** view of the solid-state molecular structures of **1** and **2**, respectively. **Table 2** compares a selection of observed bond lengths and angles with the corresponding computed values at B3LYP/6-311++G(d,p) approximation. The optimized molecular structures of **1** and **2** are shown in **Figure S1, ESI**. The optimized molecular geometries of both molecules agree well with that observed from the X-ray structural studies.

As shown in Table 2, the small differences between observed and computed geometrical parameters in compounds **1-2** can be attributed to the fact that theoretical calculations have been performed assuming isolated molecules (in gas-phase) whereas the experimental values correspond to the solid state where the intermolecular interactions play an important role. Molecules **1** and **2** are structurally closed related and isostructural to each other. Both compounds crystallize in the monoclinic space group $P2_1/c$, with one molecule in the asymmetric unit. The amide unit [-C(O)-NH-] is twisted with respect to both 2,3-dihydro-1-H-pyrazol-4yl and 2-halophenyl ring, with dihedral angles of 61.34 and 55.99º, respectively in **1**, 66.70 and 59.63º in **2**. The dihedral angles between the 2,3-dihydro-*1H*-pyrazol-4yl and 2-halophenyl rings are 12.19 and 11.64º for compounds **1** and **2**, respectively, while 2,3-dihydro-1-H-pyrazol-4yl and phenyl rings subtend dihedral angles of 43.77º for **1** and 46.55º for **2**. The rotation of the amide group with respect to both the 2-bromophenyl and 2-chlorophenyl rings are due to steric repulsion between the halogen and the O-atom from the carbonyl group. In addition, the conformation adopted between the amide group and the 2-halophenyl rings in both compounds are stabilized by intramolecular O···X halogen bonds, with Br1···O1 and Cl1···O2 distances of 3.237(2) and 3.194(3) Å, respectively. The C-N imide bond lengths equal to 1.346(3) and 1.347(4) Å for **1** and **2**, respectively, are considerably shorter than expected for single C(sp^2)-N(sp^2) bonds, whose reported average length is 1.472(5) Å **[34]** and the carbonyl bond lengths are in the range expected for imide carbonyl bonds. This feature can be attributed to the importance of resonance structures in this type of compounds. The C=O bond lengths corresponding to the 2,3-dihydro-1-H-pyrazol-4yl ring are 1.241(2) and 1.237(3) Å for compounds **1** and **2**, respectively. The N3-N2-C13 and N2-N1-C1 angles are 118.3(1) and 118.1(2)º for compounds **1** and **2**. These values are significantly smaller than the ideal value of 120º expected for N-atoms with sp^2 hybridization. These results could be probably attributed to the repulsion between the nitrogen lone pairs and the adjacent N-N bond. In general, the

geometrical parameters of both compounds are in good agreement with related compounds reported in literature **[35-39]**.

Table 2: Selected experimental (X-ray) and calculated [B3LYP/6-311++G(d,p)] geometrical parameters for compounds **1** and **2**.

Compound 1	**Exp.**	**Calc.**	**Compound 2**	**Exp.**	**Calc.**
C3-Br1	1.898(2)	1.909	C14-Cl1	1.734(3)	1.755
C2-C1	1.504(3)	1.509	C13-C12	1.502(3)	1.509
C1-O1	1.227(2)	1.224	C12-O2	1.215(3)	1.224
C1-N1	1.346(3)	1.369	C12-N3	1.347(4)	1.370
C8-N1	1.412(2)	1.397	C8-N3	1.417(3)	1.397
C8-C11	1.367(3)	1.363	C8-C9	1.364(3)	1.363
C8-C9	1.431(3)	1.460	C7-C8	1.427(4)	1.460
C9-O2	1.241(2)	1.230	C7-O1	1.237(3)	1.230
C9-N2	1.394(2)	1.394	C7-N1	1.392(3)	1.394
C11-N3	1.363(2)	1.412	C9-N2	1.364(3)	1.412
N3-N2	1.407(2)	1.415	N2-N1	1.401(3)	1.415
C10-N3	1.473(2)	1.473	C10-N2	1.473(4)	1.473
C13-N2	1.420(2)	1.419	C1-N1	1.422(3)	1.419
Br1···O1	3.237(2)	3.179	Cl1···O2	3.194(3)	3.141
C2-C1-N1	115.6(2)	113.3	C13-C12-N3	115.5(2)	113.1
C1-N1-C8	122.0(2)	130.6	C12-N3-C8	121.6(2)	130.5
N1-C8-C9	122.0(2)	113.9	N3-C8-C7	122.0(2)	114.0
N1-C8-C11	129.3(2)	137.1	N3-C8-C9	128.6(2)	137.0
N3-N2-C13	118.3(1)	119.8	N2-N1-C1	118.1(2)	119.8
C3-C2-C1-N1	127.9(2)	132.4	C14-C13-C12-N3	-123.8(3)	-131.6
C2-C1-N1-C8	163.3(2)	172.8	C13-C12-N3-C8	-163.4(2)	-172.6
C1-N1-C8-C9	-106.1(2)	-163.2	C12-N3-C8-C7	102.1(3)	162.4

The crystal packing of both compounds **1-2** is stabilized by intermolecular N-H···O hydrogen bonds involving the O-atom of the pyrazol carbonyl group and the H-atom of the amide group, leading to the formation of inversion dimers with $R_2^2(10)$ graph-set ring motif (Figures 1b and 2b, Table 3). Both structures are further stabilized by C-H···O hydrogen bonds, as shown in Figures 1 and 2. The H6A and H17 atoms interact with the O-atoms of the pyrazole ring through C-H···O hydrogen bonds giving $R_2^2(18)$ graph-set motifs (Figures 1d, 2c). The supramolecular assembly of both compounds is further stabilized by C-H···π interactions. For

compound **1**, the C16-H16A···Cg3 interactions (H16A···Cg3 distance = 2.97 Å, C16A-H16A···Cg3 angle = 141º) involve the centroid Cg3 (C13-C18) and the H16A of the phenyl ring. On the other hand, for compound **2**, C4-H4···Cg2 contacts (H4···Cg2 distance = 3.00 Å, C4-H4···Cg2 angle = 143º) involve the benzene ring (C1-C6) and the H4 of the phenyl ring of other molecule.

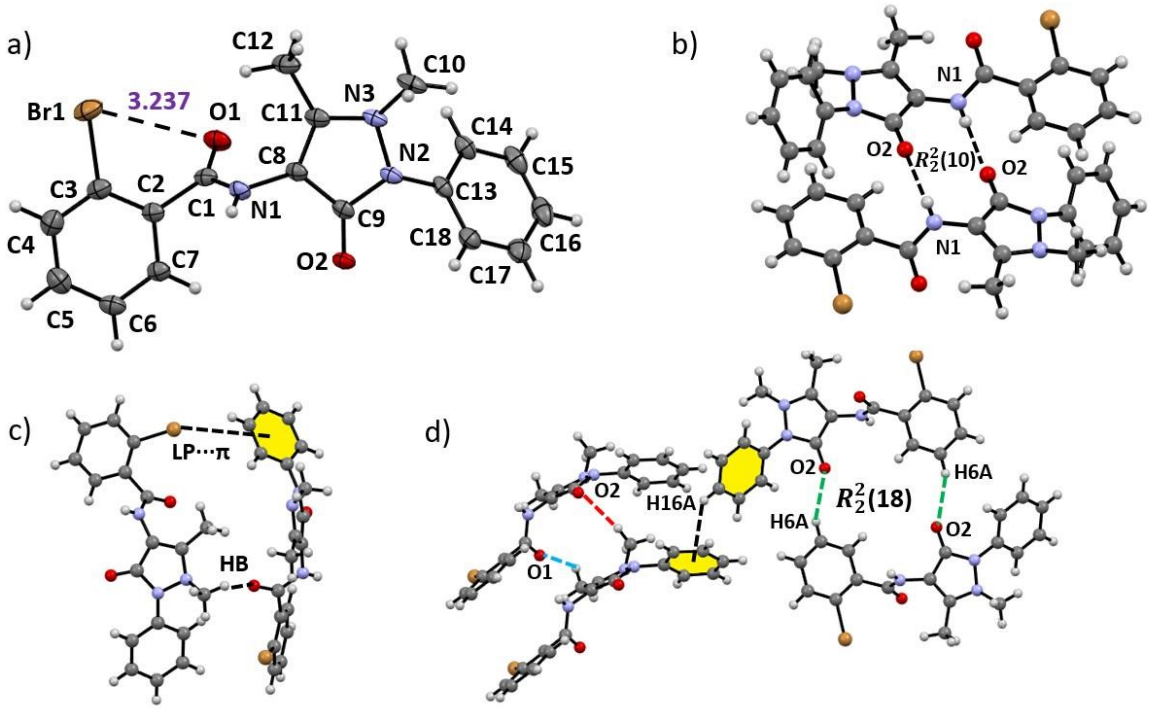

Figure 1. a) Molecular structure of **1** with displacement ellipsoids drawn at the 30% probability level, intramolecular non-bonding contacts shown as dashed lines, b) intermolecular N-H···O interactions as dashed lines, c) combination of H-bonds and lone pair···π interactions, d) formation of C-H···O hydrogen bonds and C-H···π interactions.

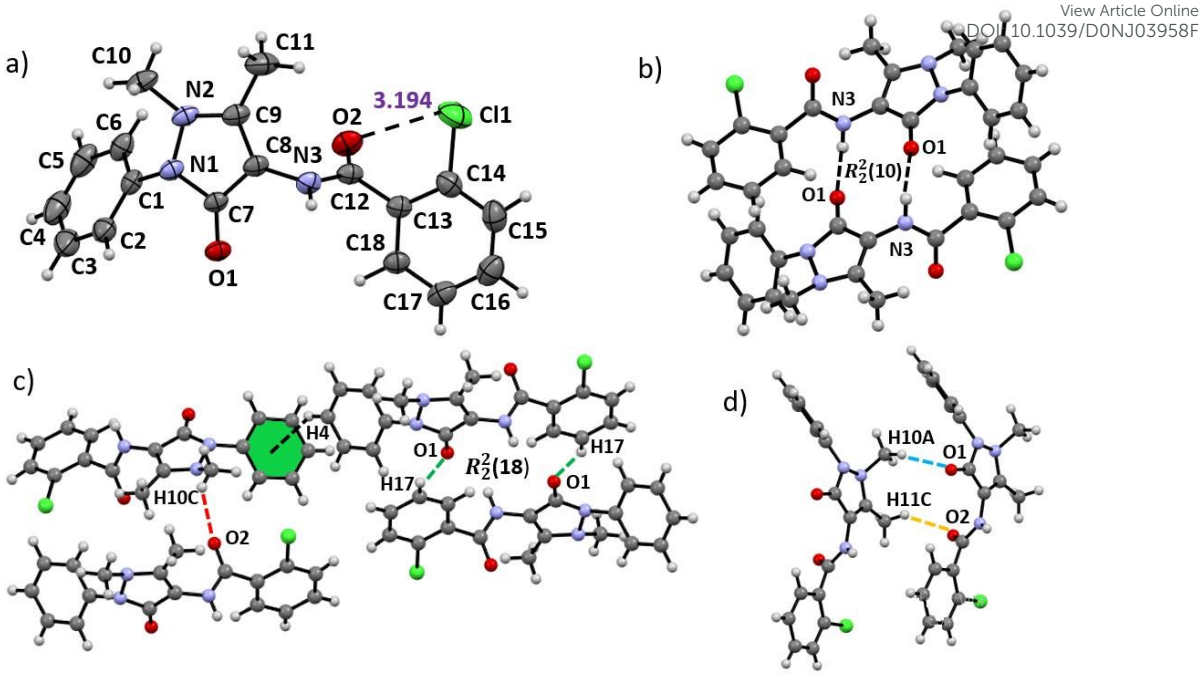

Figure 2. a) Molecular structure of **2** with displacement ellipsoids drawn at the 30% probability level. Intramolecular non-bonding contacts shown as dashed lines, b) intermolecular N-H···O interactions as dashed lines, c) formation of C-H···O hydrogen bonds and C-H···π interactions, d) formation of C-H···O H-bonds.

Interestingly, the Cg3 and Cg2 centroids for **1** and **2** are respectively linked to the halogen atom through lone pair···π interaction. For **1**, the distance between the bromide Br1 atom and the centroid Cg3 of the π face is 4.477 Å [α C3-Br1···Cg3 = 158.1º] (Figure 1c). The shorter separation distance Br1···C15 = 3.5280(2) Å and the value of angle α indicate significant lone pair ···π interactions **[40]**. Similar results were obtained for **2**, with Cl1···Cg2 distance of 4.550 Å [α C14-Cl1···Cg2 = 159.7º, Cl1···C5 distance = 3.573 Å].

Table 3: Geometrical parameters (Å, º) of the hydrogen bonds in compounds **1-2**.

D-H···A	D-H	H···A	D···A	< (D-H···A)
Compound 1				
N1-H1···O2^{i}	0.88	1.93	2.805(2)	171
C6-H6A···O2^{ii}	0.95	2.54	3.418(3)	154
C10-H10A···O1^{iii}	0.98	2.39	2.981(3)	118

View Article Online
DOI: 10.1039/D0NJ03958F

C10-H10C···O2^{iv}	0.98	2.46	3.403(2)	160
C12-H12A···O1^{iv}	0.98	2.47	3.207(3)	132
Compound 2				
N3-H3N···O1^{v}	0.890(3)	1.945(3)	2.833(3)	175
C10-H10C···O2^{vi}	0.901(3)	2.510(3)	3.037(3)	118
C11-H11C···O2^{vii}	0.952(3)	2.559(3)	3.233(3)	128
C10-H10A···O1^{vii}	1.000(3)	2.531(3)	3.479(3)	158
C17-H17···O1^{viii}	0.904(3)	2.656(3)	3.497(3)	155

Symmetry codes: (i) -x,-y,-z; (ii) -x, 2-y, -z+1; (iii) -x, y-1/2, -z+3/2; (iv) x, y-1, z; (v) –x+1, -y, -z; (vi) –x+1, +y+1/2, -z+1/2; (vii) x, +y+1, +z; (viii) –x+1, -y-1, -z.

3.2. Hirshfeld surface analysis

The Hirshfeld surfaces of compounds **1-2** showed in **Figure 3** were mapped over d_{norm}, *shape index* and *curvedness* properties and illustrate the nature and extent of different intermolecular interactions. The short and dominant intermolecular contacts are shown as bright red areas in the Hirshfeld surface mapped over d_{norm} function indicating the existence of hydrogen bonds. The two near and larger red spots labeled 1 in the d_{norm} map of both compounds are due to the formation of dimers via N1-H1···O2 (**1**) and N3-H3···O1 (**2**) bonds. These hydrogen bonds involve the acceptor O atom from the carbonyl group of the pyrazole ring. A similar pattern of bright red areas attributed to N-H···O hydrogen bonds was observed in a new o-hydroxyphenyl diazepine derivative in which the crystal packing is mainly influenced by this type of hydrogen bonds **[41]**. These contacts (Figure 1b and 2b) represent the stronger hydrogen bonding interactions in the crystal packing, as was reflected in the geometrical parameters listed in Table 3. The red regions labeled 2 in the d_{norm} maps are attributed to C10-H10A···O1 (**1**) and C11-H11C···O2 (**2**) hydrogen bonds. The deep red areas labeled 3 and 4 in the Hirshfed surface of **1** are attributed to C10-H10C···O2 and C12-H12A···O1 bonds involving the O-atoms from the pyrazole ring and amide groups, respectively. The d_{norm} map of **1** shows two red spots labeled 3 and 5 respectively attributed to C10-H10A···O1 and C10-H10C···O2 bonds. In addition, visible red spots labeled 6 (**1**) and 4 (**2**) in the d_{norm} surfaces are respectively attributed to C6-H6A···O2 and C17-H17···O1 bonds, involving the O-atom of the pyrazole ring as

View Article Online
DOI: 10.1039/D0NJ03958F

acceptor and the H atom of the 2-halophenyl ring to form graph-set motifs $R_2^2(18)$, as shown in Figures 1 and 2. The Hirshfeld surface of **1** shows small red spots (labeled 5) associated with lone pair···π interactions involving the lone pair of the bromine atom and the Cg3 centroid, as described previously. The red spot labeled 6 in the d_{norm} surface of **2** could be attributed to O2···C10 tetrel bonding interactions, with d(O2···C1) = 3.037 Å **[42]**.

Furthermore, the Hirshfeld surfaces were mapped with *shape index* and *curvedness* functions to evaluate the presence of π···π stacking interactions, which are not clearly visible in the analysis of the crystal structure **[43]**. In the *shape index* diagram of both compounds (Figure 3, column 2), the pattern of convex blue and concave red triangles, highlighted in red, indicate the existence of π-stacking interactions in the structure of both compounds, involving the 2-halophenyl ring. In accordance with the structural results, the π···π stacking interactions involve the pyrazole ring (centroid Cg1) and the 2-bromophenyl (centroid 2) and 2-chlorophenyl (centroid 3) rings, with Cg···Cg distances of 4.7189(5) for **1** and 4.6696(4) Å for **2**. These interactions are also visible as relatively large and green flat regions delineated by the red circle on the *curvedness* surfaces of both compounds (Figure 3, column 3).

	d_{norm}		***Shape index***	***Curvedness***
Compound 1	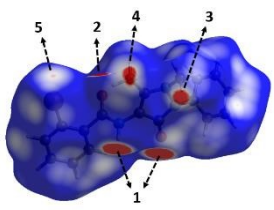	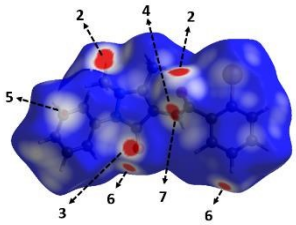	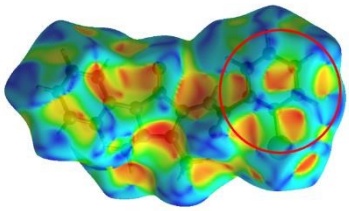	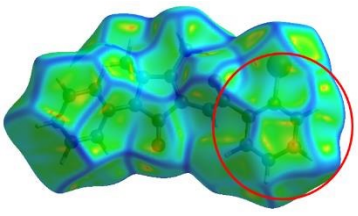
Compound 2	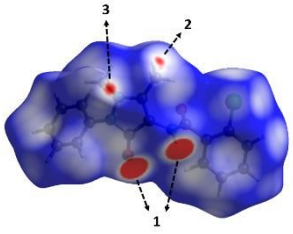	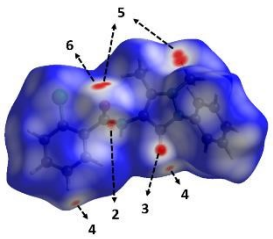	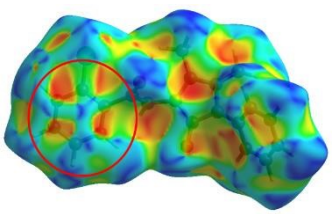	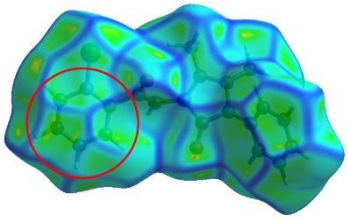

View Article Online
DOI: 10.1039/D0NJ03958F

Figure 3. Hirshfeld surfaces of compounds **1-2** mapped with d_{norm} (with the molecule in two different orientations), *shape index* and *curvedness*. For description of labels and highlighting circles, see the text.

The full 2D fingerprint plots of the main intermolecular interactions of the compounds are depicted in **Figure 4**. The van der Waals forces (H···H intermolecular contacts) are in the middle of scattered points, with minimum values of (de + di = 2.4 Å) and have a major contribution to the crystal packing of **1** (39.2%) and **2** (40.6%). The closest H···O/O···H contacts (labeled 1) are represented on the fingerprint plots by characteristic sharp spikes at de + di = 1.8 Å contributing 16.8 and 17.4% of the total Hirshfeld surface area.

The H···C/C···H contacts (labeled 2) comprise 26.7% (**1**) and 25.8% (**2**) of the total Hirshfed surface area. As shown in the fingerprint plots of both compounds, the pair of "wings" highlighted in red, indicate the existence of C-H···π intermolecular contacts, as described previously **[44]**. The broad spikes labeled 3 and 4 in the fingerprint plots are attributed to H···Br/Br···H (12.5%) for **1** and H···Cl/Cl···H (12.3%) for **2**. In addition, the fingerprint plots of both compounds show C···X/X···C contacts associated to lone pair ··· π interactions described previously.

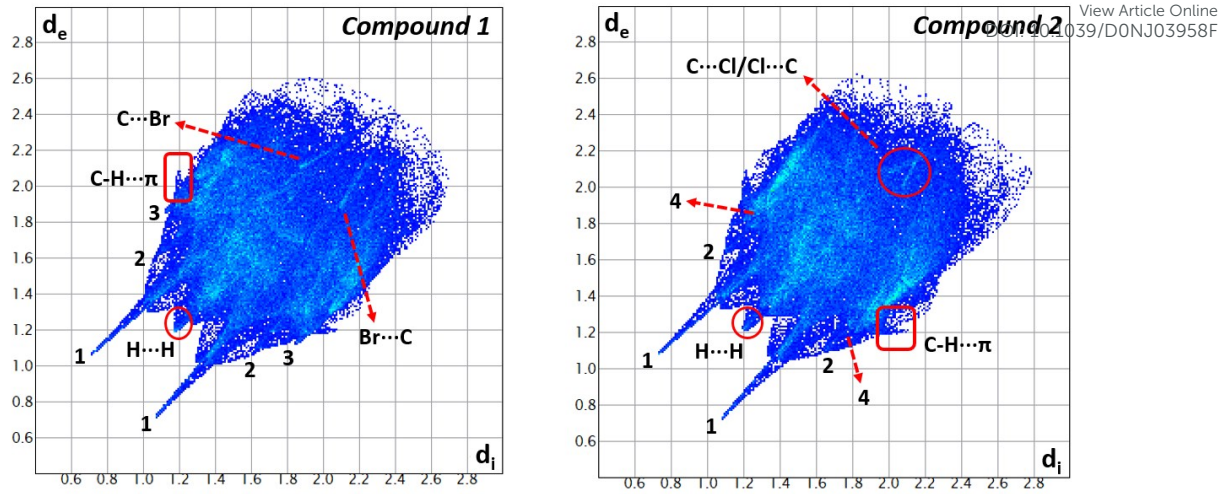

Figure 4. Full 2D fingerprint plots of compounds **1-2** showing (1) H···O/O···H, (2) H···C/C···H, (3) H···Br/Br···H, (4) H···Cl/Cl···H contacts.

3.3. Enrichment ratio

The enrichment ratios (Exy) of contacts between the different chemical species X and Y were calculated from the chemical composition on the Hirshfeld surface to highlight which contacts are statically favored and kept in the crystal packing of the compounds **[45]**. The E_{XY} is defined as a ratio between the proportion of actual contacts C_{XY} in the crystal and the theoretical proportion of random contacts R_{XY}. The C_{XX} and C_{XY} values are used to calculate the proportion S_X of different chemical species on the molecular surface. The random contacts R_{XY} were computed from the corresponding S_X and S_Y proportions by using of probability products. Enrichment ratios larger than unity indicate that these contacts are over-represented in the crystal packing with respect to the chemical composition on the Hirshfeld surface. The chemical species that tend to avoid contacts are represented by enrichment values lower than unity **[45]**.

The E_{XY} values for the compounds are presented in **Table 4**, and the complete information is provided in **Table S1, ESI**. The largest contributions to the Hirshfeld surfaces

are from H···C/C···H, H···O/O···H and H···X/X···H (X= Br, Cl) and their enrichment ratio values are in the 1.3-1.4 range, with the same values for both compounds. The computed E_{XY} values are significantly higher than unity, showing high propensity to form C-H···π, C-H···O or N-H···O and C-H···X hydrogen bonds, as result of high and most proportion S_H of hydrogen atoms at the molecular surface. The propensity of the 2-halophenyl and pyrazole rings to form π···π stacking interactions is much more extensive in **2**, as reflected by the highly increased $E_{CN/NC}$ values of 1.75 and 2.3, respectively, which are associated to C···N/N···C contacts **[43b, 46]**. These results indicate that the π···π stacking interactions are more favored in **2**, in accordance with the geometrical parameters of the π···π stacking interactions of both compounds **[43b, 46]**. For **2**, the value of Cg1···Cg3 inter-centroid distance of 4.6696(4) Å is lower as compared with Cg1···Cg2 inter-centroid distance of 4.7189(5) Å observed in **1**. These results indicate that the π···π stacking interactions in **1** are weaker. On the other hand, the likelihood to form N···O/O···N contacts are high in the crystal packing, with E_{NO} values of 1.40 (**1**) and 1.50 (**2**). The E_{NH} and E_{CC} values show that N···H and C···C contacts are slightly favored, whereas the C···O/O···C contacts are practically avoided.

Table 4: Enrichment ratios (E_{XY}) of the main intermolecular interactions for compounds **1-2**.

Interaction	**E_{XY}**	
	Compound 1	***Compound 2***
H···H	0.85	0.85
H···C/C···H	1.3	1.3
H···N/N···H	0.9	0.9
H···O/O···H	1.4	1.4
H···X/X···H	1.3	1.3
C···C	0.09	0.1
C···O/O···C	0.04	0.04
C···N/N···C	1.75	2.3
C···X/X···C	0.9	0.7
N···O/O···N	1.4	1.5

3.4. Energy frameworks

The energy frameworks of compounds **1-2** were calculated with *CrystalExplorer*17.5 program **[26]** using the HF/3-21G approximation. Quantification of the framework energies is an important method for understanding the topology of the overall interactions of molecules in the crystal packing. This technique provides information about the types of energy responsible for the supramolecular assembly in the solid. The interaction energies between pair of molecules are described as the sum of electrostatic (E_{ele}), polarization (E_{pol}), dispersion (E_{dis}) and exchange-repulsion (E_{rep}) terms **[47]**. A cluster of molecules within a radius of 3.8 Å for a central molecule was generated **[47]**. The scale factors used are 1.019, 0.651, 0.901 and 0.811 for electrostatic, dispersion, polarization and repulsion interactions, respectively **[48]**. **Figure 5** shows the energy frameworks constructed with the calculated interaction energies for **1** and the frameworks of **2** are shown in **Figure S2, ESI**. The interaction energies for selected molecular pair of compounds **1-2** are presented in Table 5.

From **Table 5**, it can be appreciated that the highest total energies of -87.8 kJ/mol (**1**) and -86.7 kJ/mol (**2**) correspond to the molecular pair formed by N-H···O bonds generating $R_2^2(10)$ ring motifs (see Figures 1b and 2b) being the shorter contact and the strongest interaction of all the hydrogen bonds that are responsible of the crystal packing of **1** and **2**. These results are in agreement with the geometrical parameters shown in Table 3 and with the energetic values obtained for the same interactions in a related compound **[49]**. On the other hand, the N-H···O bonds shows a relatively high electrostatic energy of -81.6 kJ/mol (**1**) and -76.8 kJ/mol (**2**). The second important contribution (of about 18 %) to the total energy is for pair of molecules with E_{tot} values of -42.3 kJ/mol (**1**) and -41.8 kJ/mol (**2**), associated with C-H···O bonds. For **2**, the pair of molecules interacting with E_{tot} value of -36.7 kJ/mol involves C17-H17···O1 bonds, with an important contribution of electrostatic energy (-19.3 kJ/mol), in agreement with reported values **[49]**. For **1**, the total energy of -37.9 kJ/mol involves C-H···O and C-H···Br bonds, as shown in Table 5. In **1**, the molecular pair with total energy value of -

View Article Online
DOI: 10.1039/D0NJ03958F

36.7 kJ/mol involves C6-H6A···O2 bonds and the presence of C-H···π interaction, which further increases the stability of the dimer. These features may also explain the dominance of the dispersion energy in the molecular pair as a result of the attractive dispersive nature of π-interactions **[50]**.

From the analysis of the energy frameworks we have extracted net energies. For both compounds, the sum of dispersion energies (-237.2 kJ/mol for **1** and -211.7 kJ/mol for **2**) are greater than that of electrostatic energies (-138.5 and -128.4 kJ/mol), hence indicating that remarkably dispersion energy dominates over the electrostatic energy, as shown in the thickness of the cylinders along the *c*-axis. **Figure 5** clearly indicates that the electrostatic energy frameworks are relevant from the dimers stacked along the *a*-axis and *b*-axis as can be seen by thick cylinders linking molecules **[47, 48]**.

Compound 1

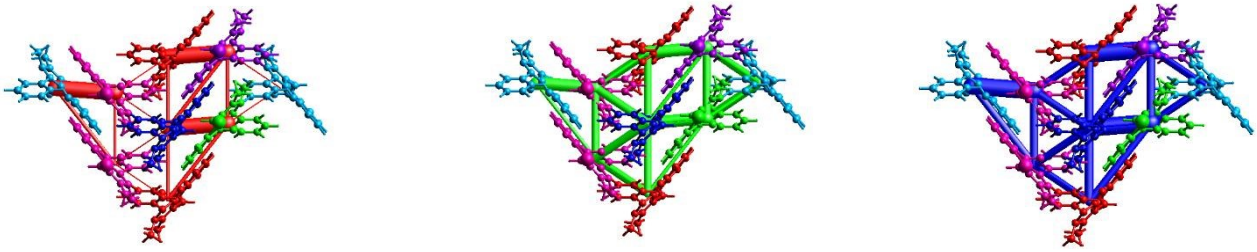

a-axis

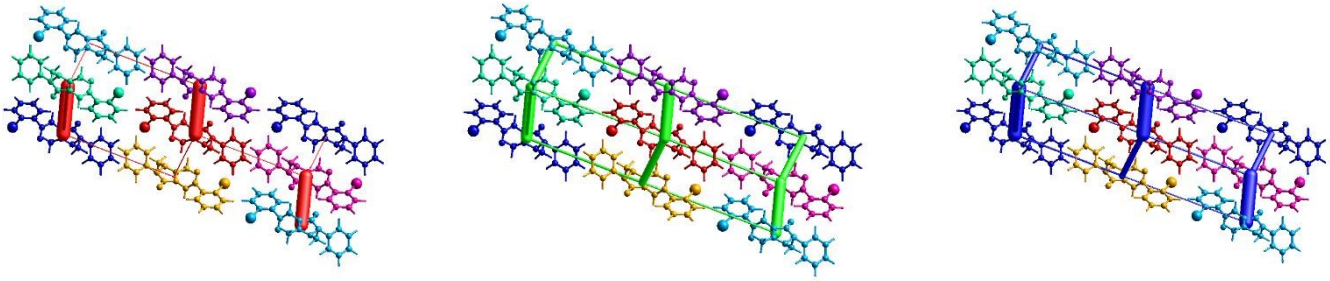

b-axis

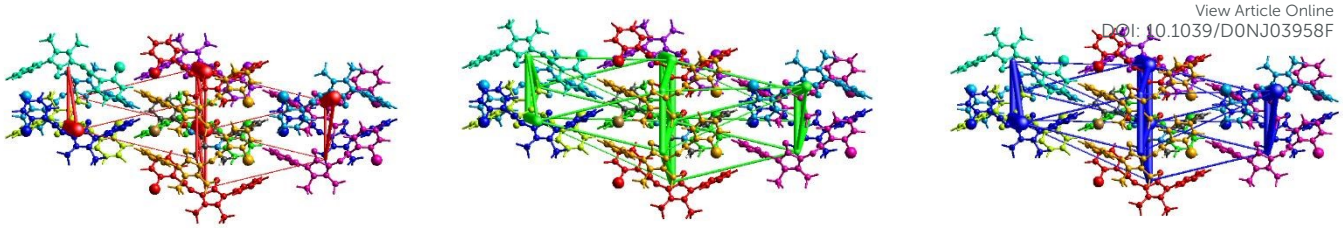

c-axis

Figure 5. Energy frameworks along *a*-axis (above), *b*-axis (middle), *c*-axis (botton) for compound **1**, showing separate electrostatic (left, red), and dispersion (middle, green) components, and total energy interactions (right, blue). The tube size (scale factor) used in all energy frameworks was 90 and the cut-off was 5.00 kJ/mol.

Table 5: Interaction energies (E_{tot}) partitioned into electrostatic (E_{ele}), polarization (E_{pol}), dispersion (E_{dis}) and exchange-repulsion (E_{rep}) contributions (kJ/mol) for selected molecular pairs.

A	N[b]	Symmetry code	R[c]	Interactions	d(H···A/Cg)[d], < D-H···A	E_{ele}	E_{pol}	E_{dis}	E_{rep}	E_{Tot}
Compound 1										
	2	x, y, z	6.11	C12-H12A···O1 C10-H10C···O2	2.473(3), 131 2.464(3), 160	-17.1	-6.6	-45.9	25.5	-42.3
	2	-x, y+1/2, -z+1/2	5.88	C10-H10A···O1 C10-H10A···Br1 C15-H15A···Br1	2.393(3), 118 3.906(3), 95.48 3.084(3), 110,31	-5.9	-14.0	-49.0	26.4	-37.9
	1	-x, -y, -z	12.35	C4-H4A···Br1	3.099(3), 136.98	-4.8	-0.5	-12.6	10.5	-8.0
	1	-x, -y, -z	5.41	N1-H1···O2	2.076(2), 175	-81.6	-27.1	-72.6	96.6	-87.8
	1	-x, -y, -z	13.85	H4-H5	2.40	-2.2	-0.8	-8.4	2.2	-8.6
	2	x, -y+1/2, z+1/2	15.27	H5A-H15A	2.70	0.4	-0.3	-5.3	1.0	-3.8
	2	x, y, z	14.13	Br1···Cg(3)	4.477(5)	-1.7	-0.2	-4.4	1.4	-4.7
	1	-x, -y, -z	8.28	C6-H6A···O2 C18-H18···Cg(2)	2.540(3), 154 2.920, 141	-19.8	-9.4	-22.6	12.4	-36.7
	2	-x, y+1/2, -z+1/2	15.23	C16-H16···Cg(3)	2.970(2), 139	-5.8	-1.4	-16.4	12.1	-11.8
Compound 2										
	2	x, -y+1/2, z+1/2	15.26	H4···Cg(3)	3.00	0.2	-0.2	-4.9	0.8	-3.7
	2	-x, -y, -z	14.78	H17···Cg(3)	2.70	-1.6	-0.7	-7.2	1.7	-7.1
	1	-x, -y, -z	13.38	C15-H15···Cl	2.687(0), 81.44	-4.4	-0.5	-8.9	6.2	-7.9
	1	x, y, z	13.99	C3-H3·· Cl	3.528(2), 78.8	-1.3	-0.3	-3.2	0.6	-3.9
	1	-x, -y, -z	8.05	C17-H17···O1	2.656(3), 155	-19.3	-8.7	-20.5	8.8	-36.7
	2	-x, -y, -z	5.04	N3-H3N···O1	1.945(3),175	-76.8	-25.6	-69.6	87.4	-86.7
	2	x, y, z	6.24	C10-H10A···O1 C11-H11C···O2	2.531(3), 158 2.559(3), 128	-16.0	-6.4	-41.1	19.4	-41.8
	1	-x, y+1/2, -z+1/2	5.96	C10-H10C···O2 C6-H6···O2	2.510(2), 118 2.902(2), 161.8	-4.2	-12.9	-40.9	17.6	-35.2
	2	-x, y+1/2, -z+1/2	14.08	H4 ···Cg(2)*	3.00	-5.0	-1.3	-15.4	9.9	-11.8

[a] Molecule color; [b] Number of molecules at R distance; [c] distance (Å) between molecular centroids (mean atomic position); [d] Geometry of H-bonds (Å, °) and H ···Cg distance (Å); Cg(2), Cg(2)*and Cg(3) are the centroids of the N2/N3/C11/C8/C9, N1/N2/C9/C8/C7 and C13-C18 rings, respectively.

View Article Online
DOI: 10.1039/D0NJ03958F

3.5. Theoretical study

In order to complement the energetic analysis discussed above, we have also evaluated the important motifs of compounds **1** and **2** shown in Figures **1** and **2**. For this purpose, we have performed B3LYP-D3/def2-TZVP calculations in four dimers of each compound in combination with QTAIM analysis and NCIplot calculations. Using the QTAIM analysis we have also evaluated each individual H-bond in the $R_2^2(10)$ and $R_2^2(18)$ graph-set motifs.

First of all, we have computed the molecular electrostatic potential (MEP) surface **[51]** of compound **1** (also as model of **2**) to locate the most positive and negative parts of the molecule, which is represented in **Figure 6**. It can be observed that the most positive region corresponds to the H-atoms of the amido group (+33 kcal/mol) as expected. Moreover, the H-atoms of the N–CH_3 group also exhibits a large and positive MEP value (+25 kcal/mol) thus explaining its participation in multiple C–H···O interactions in the solid state of **1** and **2**. The aromatic H-atoms are also positive (up to 16 kcal/mol, see Figure 6a). The most negative value is located at the O-atom of the pyrazolone ring (–45 kcal/mol) that is slightly more nucleophilic than the amidic O-atom (–42 kcal/mol). Finally, the MEP is negative over the phenyl rings, which present a significant anisotropy. That is, the MEP values above and below the center of the aromatic rings are quite different (up to 14 kcal/mol difference in the phenyl ring).

View Article Online
DOI: 10.1039/D0NJ03958F

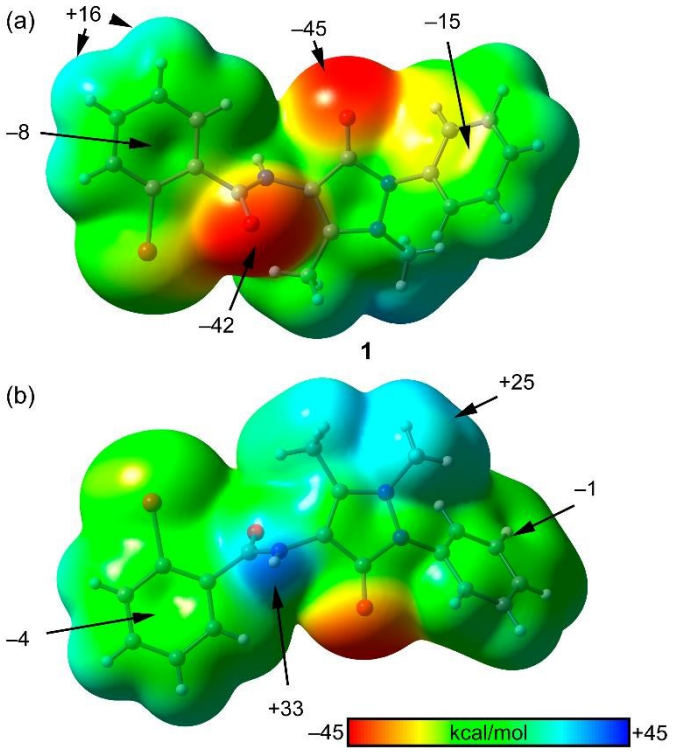

Figure 6. (a,b) Two opposite views of the MEP surface of compound **1** (iso-surface = 0.001 a.u.) at the B3LYP-D3/def2-TZVP level of theory. The energies at selected points of the surfaces are given in kcal/mol).

Figure 7 shows the QTAIM analysis **[52]** of three dimers of compounds **1** and **2**, along with the binding energies and the superposition of the NCIplot surfaces **[53]**. Those represented in Figure 6a and b correspond to the $R_2^2(10)$ and $R_2^2(18)$ graph-set motifs of **1** and the equivalent motifs of compound **2** are represented in Figure 6d and e. The QTAIM analysis confirms the existence of the H-bonds in both motifs, each one characterized by a bond critical point (CP) (red sphere) and bond path interconnecting the H and O-atoms. The NCIplot index characterizes these H-bonds as small iso-surfaces which are blue (strong interaction) in the $R_2^2(10)$ motif and green (weak interaction) in the $R_2^2(18)$ graph-set motif. This is in line with the MEP surface analysis, since the MEP value at the aromatic H-bonds is modest (up to 16 kcal/mol) compared to that at the N–H group. Agreeably, the binding energy of the $R_2^2(10)$

View Article Online
DOI: 10.1039/D0NJ03958F

motif is large (–21.4 kcal/mol in **1** and –23.2 kcal/mol in **2**) due to the strong H-bonds and additional contribution from aromatic interactions (see green iso-surfaces between the aromatic and the 3-methylpyrazolone moiety). In contrast, the $R_2^2(18)$ graph-set motif presents more modest interaction energies (–8.2 and –7.6 kcal/mol in **1** and **2**, respectively). Figures 7c,f also show additional motifs where a combination of C–H···O, C–H···π and X···π (X = Br and Cl) interactions stabilizes the dimers. These type of interactions have been previously described in the literature as recurrent forces in the solid state of a variety of compounds **[54]**. All these interactions are confirmed by the existence of the corresponding bond CPs, bond paths and NCIplot iso-surfaces. These motifs involve the methyl groups as H-bond donors, which are more positive than the aromatic H-atoms, as revealed by the MEP surface analysis. This fact likely explains the larger interaction energies obtained for these motifs (–12.2 kcal/mol for **1** and –11.9 kcal/mol for **2**). In general, the interaction energies obtained for the three motifs shown in Figure 7 are similar for Br and Cl, thus revealing that the halogen atom has a little effect on the interaction energies.

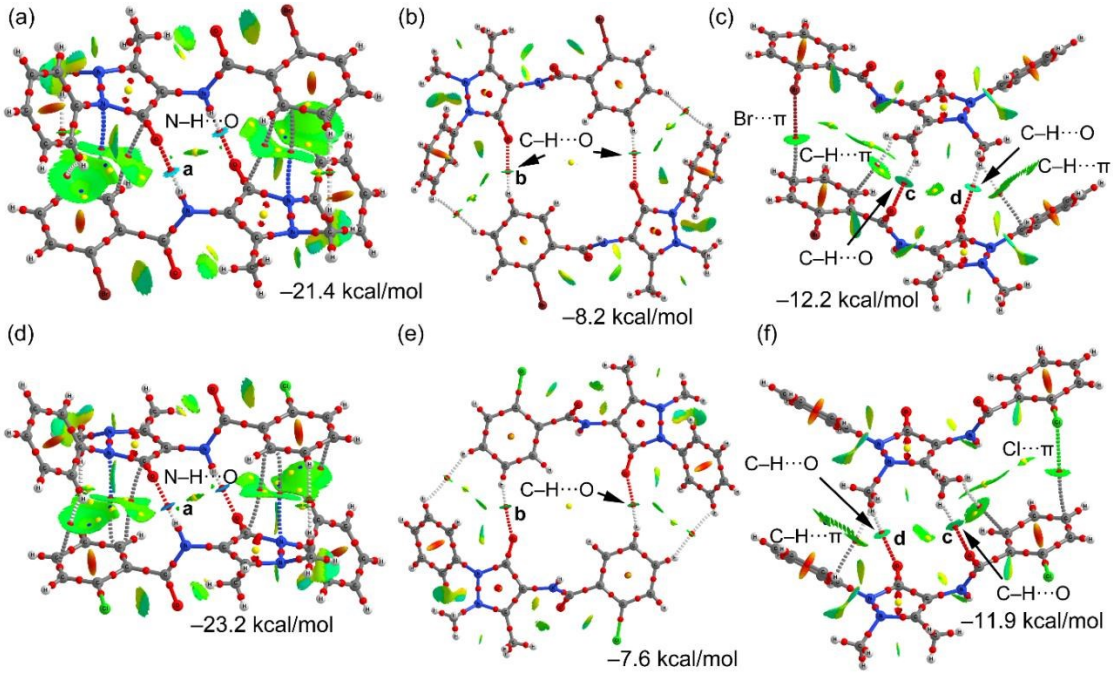

Figure 7. Combination of QTAIM (bond CP in red, ring Cp in yellow and cage CP in blue) and NCIplots of the three motifs of compound **1** (a-c) and **2** (d-f). The binding energies are also indicated.

Table 6 gathers the values or ρ(r), electronic potential energy density [V(r)] and electronic kinetic energy density [G(r)] values at the bond critical points that characterize the H-bonds, which are labeled in **Figure 7**. The dissociation energies of each H-bond based on the V(r) QTAIM parameter [E = 0.5V(r)] **[55]** have been also included in Table 6. It can be observed that for the $R_2^2(10)$ motif the sum of the contributions of both H-bonds is –8.8 kcal/mol in **1** and –12.2 kcal/mol for **2**, thus confirming that these H-bonds are the strongest ones in agreement with the NCIplot and MEP surface analysis. The stronger energies computed for **2** are in good agreement with the experimental geometric features of the H-bonds (see Table 3), which indicate shorter H···O and longer N–H distances in compound **2** as compared to **1**. It is worthy to highlight that in these $R_2^2(10)$ motifs, the sum of the other forces (π–interactions and other long-range interactions) is also very important. This contribution can be roughly estimated by subtracting the QTAIM energies corresponding to the H-bonding to the total interaction energies of the dimers [–21.4 –(–8.8) = –12.6 kcal/mol in **1** and –23.2 –(–12.2) = –11.0 kcal/mol in **2**]. For the $R_2^2(18)$ motif the H-bonding contribution is only –2.4 kcal/mol in **1** and –1.8 kcal/mol in **2**, thus evidencing that these H-bonds are very weak, also in agreement with the NCIplot. Finally, the H-bonds involving the methyl groups (CPs c and d) are stronger than those involving the aromatic rings, in agreement with the MEP analysis. The –V(r) values are smaller than the G(r) values at the bond CPs, thus confirming the noncovalent nature of the H-bonds.

Table 6. QTAIM ρ(r), V(r) and G(r) parameters at the bond CPs labelled in Figure 7 in a.u. and predicted dissociation energies for each interaction using the electronic potential energy densities.

Compound	CP	ρ(r)	V(r)	G(r)	E_{dis} (QTAIM)
1	a	0.0180	–0.0139	0.0180	4.4
	b	0.0068	–0.0038	0.0053	1.2
	c	0.0096	–0.0057	0.0076	1.8
	d	0.0090	–0.0049	0.0066	1.5
2	a	0.0240	–0.0193	0.0226	6.1
	b	0.0053	–0.0029	0.0041	0.9
	c	0.0082	–0.0048	0.0064	1.5
	d	0.0078	–0.0041	0.0056	1.3

Finally, two additional dimers dominated only by C–H···π interactions observed in the solid state of both complexes have been analyzed (see Figure 8) energetically and using the QTAIM/NCIplot computational tools. In both compounds the C–H···π interaction is characterized by two bond CPs and bond paths connecting the aromatic H-atoms to two C-atoms of the phenyl ring. The NCIplot shows a green iso-surface located between the aromatic ring and both H-atoms, further confirming the existence and attractive nature of the interaction. The dimerization energies are similar for both compounds (–3.0 kcal/mol in **1** and –3.1 kcal/mol in **2**) and in the range of energy interactions found for related organic compounds **[48]**.

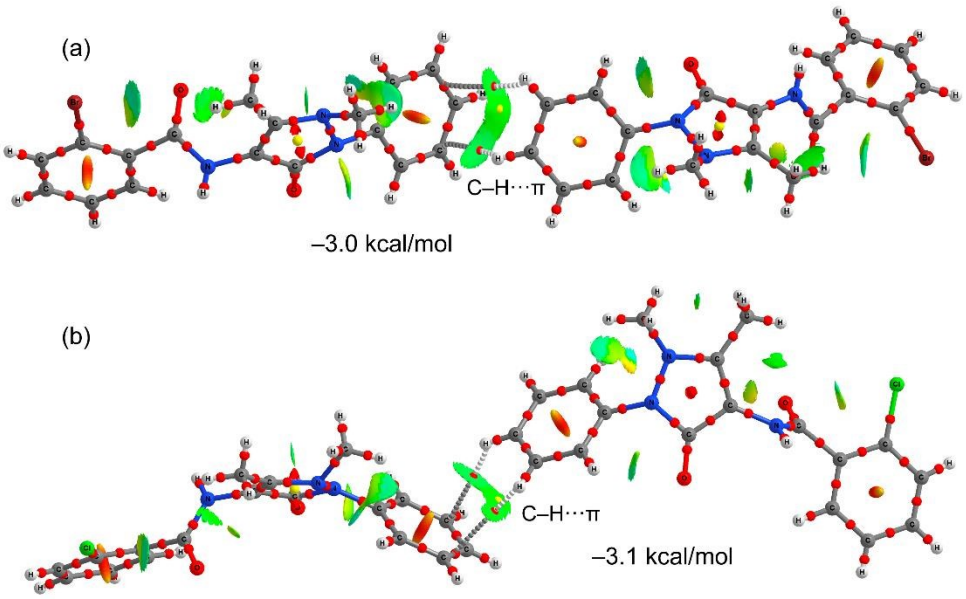

View Article Online
DOI: 10.1039/D0NJ03958F

Figure 8. Combination of QTAIM (bond CP in red and ring CP in yellow) and NCIplots of the C–H···π motifs of compound **1** (a) and **2** (b). The binding energies are also indicated.

4. Conclusions

Two novel phenazone derivatives have been synthesized and characterized, showing the capability of obtaining phenazone-hybrid compounds through the reaction of 4-aminophenazone and acyl halides. Their crystal structures were solved by X-ray diffraction methods. The compounds are isostructural to each other and crystallize in the monoclinic $P\,2_1/c$ space group, with Z= 4. The halo substitution of the phenyl ring in the position 2 leads to the adoption of a conformation in which the amide group and the 2-halophenyl rings interact *via* intramolecular O···X halogen bonds, with Br1···O1 and Cl1···O2 distances of 3.237(2) and 3.194(3) Å, respectively. Moreover, the crystal packing is also affected by the presence of the 2-halophenyl group through significant lone pair···π interaction.

The crystal structures of compounds **1-2** reveal that the intermolecular N-H···O, C-H···O, C-H···π and lone pair···π interactions are the main driving interactions in the supramolecular assembly formation. These interactions were studied through the Hirshfeld surface analysis to reveal the nature and their contributions to the total Hirshfeld surface area. In accordance with energy framework energy analysis, the N-H···O hydrogen bonds in both compounds play an important role in the crystal packing, where the electrostatic term is dominant. The dispersion energy values prevail over the electrostatic contribution in the calculation of the solid-state interaction energies, hence indicating that the role of C-H···π and lone pair ···π dispersion interactions are significant, as shown in the energy framework diagrams along the *c*-axis. The interactions have been analyzed by combined QTAIM and

NCIplot computational tools, which confirm the existence of such compounds and also the relevance of other interactions apart from the conventional N-H···O hydrogen bonds.

Acknowledgments

Financial support from the MICIU of Spain (project CTQ2017-85821-R FEDER funds), Consejo Nacional de Investigaciones Científicas y Técnicas, CONICET (Grant PIP 0651) and Facultad de Ciencias Exactas, Universidad Nacional de La Plata, UNLP (Grants 11/X709 and 11/X794) of Argentina is gratefully acknowledged. We thank the CTI (UIB) for computational facilities. D.M.G., M.F.E., G.A.E. and O.E.P. are Research Fellows of CONICET. M.R. thanks CONICET for a post-doctoral fellowship.

Electronic Supplementary Information. The general mechanism for synthesis of benzamide derivatives of 4-aminophenazone is given in Scheme S1. The optimized molecular structures of compounds **1** and **2** are shown in Figure S1. Figure S2 shows the energy frameworks along crystal axis for compound **2**. Table S1 lists the Hirshfeld contact surfaces, proportion of chemical type on the molecular surface and random contacts of the main intermolecular interactions for compounds **1** and **2**.

References

1. Y-X. Sun, W.-X. Wei, Q.-L. Hao, L.-D. Lu, X. Wang. *SpectrochimicaActa* Part A. 2009, **73**, 772-781.
2. R. Bluth. *Pharmazie*. 1982, **37**, 441-443.
3. F. de Campos, R. Correa, M.M.D. Souza, R.A. Yunes, R.J. Nunes, V.C. Filho. *Arzneimittelforschung*, 2002, **52**, 455-461.
4. D. Romer, *Br. J. Clin. Pharmacol.*. 1980, 2, 247S-251S.
5. R.M. Srivastava, R.A. Filho, W., C.A. da Silva, A. Bortoluzzi. J. *Ultrason. Sonochem.*. 2009, **16**, 737-742.

6. M. Himaja, K. Rai, K.V. Anish, M.V. Ramana, A.A. Karigar. *J. Pharm. Sci. Innov.* 2012, **1**, 67-70.
7. A.I.M. De Sutter, M.L. van Driel, A.A. Kumar, O. Lesslar, O.A. Skrt. Cochrane Db. Syst. Rev., 2012, **2**, Art. No.: CD004976.
8. S. Murtaza, M. S. Akhtar, F. Kanwal, A. Abbas, S. Ashiq, S. Shamim. *J. Saudi Chem. Soc.* 2017, **21**, S359-S372.
9. A. M. Asiri, S. A. Khan. Synthesis and anti-bacterial activities of some novel schiff bases derived from aminophenazone. *Molecules*, 2010, **15**, 6850-6858.
10. A. Shaabani, E. Soleimani, A.H. Rezayan. *Tetrahedron Lett*. 2007, **48**, 6137-6141.
11. S.A.F. Rostom, I.M. El-Ashmawy, H.A. Abd El Razik, M.H. Badr, H.M.A. Ashour, *Bioorganic. Med. Chem*. 2009, **17**, 882–895.
12. G. Gilli, P. Gilli, The Nature of Hydrogen Bond, Oxford University Press, Oxford, 2009.
13. J.M. Lehn, Supramolecular Chemistry: Concepts and Perspectives, Wiley-VCH, Weinheim, 1995.
14. Z. Setifi, D. Zambon, F. Setifi, M. El-Ghozzi, R. Mahiou, C. Glidewell, *Acta Crystallogr*. 2017, **C73**, 667-673.
15. G. Cavallo, P. Metrangolo, R. Milani, T. Pilati, A. Priimagi, G. Resnati, G. Terraneo, *Chem. Rev*. 2016, **116**, 2478-2601.
16. G.C. Pimentel, A.L. McClellan, The Hydrogen Bond; W.H. Freeman & Co: San Francisco, USA, 1960.
17. P. Hobza, K. Müller-Dethlefs, Noncovalent Interactions. Theory and Experiments, RSC Thepretical and Computational Chemistry Series, Cambridge, 2010.
18. T. Clark, M. Hennemann, J.S. Murray, P. Politzer, *J. Mol. Model*. 2007, **13**, 291-296.
19. J.S. Murray, P. Lane, T. Clark, K.E. Riley, P. Politzer, *J. Mol. Model.* 2012, **18**, 541-548.
20. M.N. Ahmed, K.A. Yasin, S. Aziz, S.U. Khan, M.N. Tahir, D.M. Gil, A. Frontera, *CrystEngComm*, 2020, **22**, 3567-3578.
21. CrysAlisPro, Oxford Diffraction Ltd., version 1.171.37.31 (release 14-01-2014 CrysAlis171.NET). CrysAlisPro, Agilent Technologies.
22. G. M. Sheldrick, *Acta Cryst*. 2008, **A64**, 112-122.
23. (a) M.A. Spackman, D. Jayatilaka, *CrystEngComm*, 2009, **11**, 19-32; (b) J.J. McKinnon, M.A. Spackman, A.S. Mitchel, *Acta Crystallogr*. 2004, **B60**, 627-668; (c) Y. H. Luo, C.

Chen, D.L. Hong, X.T. He, J.W. Wang, B.W. Sun, *J. Phys. Chem. Lett*. 2018, **9**, 2158-2163.

24. (a) J.J. McKinnon, D. Jayatilaka, M.A Spackman, *Chem. Commun*. 2007, 3814-3816; (b) M.A. Spackman, Chem. Rev. 1992, **92**, 1769-1797.
25. (a) J. K. Zaręba, M. J. Białek, J. Janczak, J. Zoń and A. Dobosz, *Cryst. Growth Des*., 2014, **14**, 6143–6153; (b) E. Önal, T. M. Okyay, G. Ekineker, Ü. İşci, V. Ahsen, S. Berber, Y. Zorlu and F. Dumoulin, *J. Mol. Struct*., 2018, **1155**, 310–319; (c) D. Pogoda, J. Janczak and V. Videnova-Adrabinska, *Acta Crystallogr., Sect. B: Struct. Sci., Cryst. Eng. Mater.*, 2016, **72**, 263–273; (d) A. Bulut, M. Worle, Y. Zorlu, E. Kirpi, H. Kurt, J. Zubieta, S. Grabowsky, J. Beckmann and G. Yucesan, *Acta Crystallogr., Sect. B: Struct. Sci*., 2017, **73**, 296–303; (e) A. Pietrzak, J. Modranka, J. Wojciechowski, T. Janecki and W. M. Wolf, *Cryst. Growth Des*., 2018, **18**, 200–209; (f) A. Saeed, U. Flörke, A. Fantoni, A. Khurshid, H. Pérez, M.F. Erben, *CrystEngComm*, 2017, **19**, 1495-1508.
26. M.J. Turner, J.J. McKinnon, S.K. Wolff, D.J. Grimwood, P.R. Spackman, D. Jayatilaka, M.A. Spackman, CrystalExplorer17, 2017.
27. Gaussian 16, Revision A.03, M.J. Frisch, G.W. Trucks, H.B. Schlegel, G.E. Scuseria, M.A. Robb, J.R. Cheeseman, G. Scalmani, V. Barone, G.A. Petersson, H. Nakatsuji, X. Li, M. Caricato, A. Marenich, J. Bloino, B.G. Janesko, R. Gomperts, B. Mennucci, H.P. Hratchian, J.V. Ortiz, A.F. Izmaylov, J.L. Sonnenberg, D. Williams-Young, F. Ding, F. Lipparini, F. Egidi, J. Goings, B. Peng, A. Petrone, T. Henderson, D. Ranasinghe, V.G. Zakrzewski, J. Gao, N. Rega, G. Zheng, W. Liang, M. Hada, M. Ehara, K. Toyota, R. Fukuda, J. Hasegawa, M. Ishida, T. Nakajima, Y. Honda, O. Kitao, H. Nakai, T. Vreven, K. Throssell, J.A. Montgomery, Jr., J.E. Peralta, F. Ogliaro, M. Bearpark, J.J. Heyd, E. Brothers, K.N. Kudin, V.N. Staroverov, T. Keith, R. Kobayashi, J. Normand, K. Raghavachari, A. Rendell, J.C. Burant, S.S. Iyengar, J. Tomasi, M. Cossi, J.M. Millam, M. Klene, C. Adamo, R. Cammi, J.W. Ochterski, R.L. Martin, K. Morokuma, O. Farkas, J.B. Foresman, D.J. Fox, Gaussian, Inc., Wallingford CT, 2016.
28. S. Grimme, J. Antony, S. Ehrlich, H. Krieg, *J. Chem. Phys*. 2010, **132**, 154104.
29. S.M.N. Islam, D. Dutta, A.K. Verma, H. Nath, A. Frontera, P. Sharma, M.K. Bhattacharyya, *Inorg. Chim. Acta*, 2019, **498**, 119161.
30. R.F.W. Bader, *J. Phys. Chem*. 1998, **102**, 7314-7323.
31. J. Contreras-Garcia, E. Johnson, S. Keinan, R. Chaudret, J-P Piquemal, D. Beratan, W. Yang, *J. Chem. Theor. Comp*. 2011, **7**, 625-632.

32. AIMAll (Version 19.02.13), Todd A. Keith, TK Gristmill Software, Overland Park KS, USA, 2019 (aim.tkgristmill.com).
33. L.J. Farrugia, *J. Appl. Cryst*. 1997, **30**, 565.
34. F.H. Allen, O. Kennard, D.G. Watson, L. Brammer, A.G. Orpen, R. Taylor, *J. Chem. Soc., Perkin Trans*. 1987, **2**, S1-S19.
35. R.J. Butcher, A. Mahan, P.S. Nayak, B. Narayana, H.S. Yathirajan, *Acta Crystallogr*., 2013, **E69**, o39.
36. H.K. Fun, C-K. Quah, P.S. Nayak, B. Narayana, B.K. Sarojini, *Acta Crystallogr*., 2012, **E68**, o2677.
37. A. Mahan, R.J. Butcher, P.S. Nayak, B. Narayana, H.S. Yathirajan, *Acta Crystallogr*., 2013, **E69**, o42-o43.
38. M. Kaur, J.P. Jasinski, B.J. Anderson, H.S. Yathirajan, B. Narayama, *Acta Crystallogr*., 2013, **E69**, o1726-o1727.
39. M. Kaur, J.P. Jasinski, H.S. Yathirajan, B. Narayama, K. Byrappa, *Acta Crystallogr*., 2014, **E70**, o636-o637.
40. M. Egli, S. Sarkhel, *Acc. Chem. Res*., 2007, **40**, 197-205.
41. (a) M. Rocha, D.M. Gil, G.A. Echeverría, O.E. Piro, J.L. Jios, S.E. Ulic, *J. Org. Chem*. 2019, **84**, 11042-11053; (b) M. Rocha, G.A. Echeverría, O.E. Piro, J.J. Jios, R.D.I. Molina, M.E. Arena, S.E. Ulic, D.M. Gil, *Aust. J. Chem*. 2020, **73**, 49-60; (c) A. Saeed, S. Ashraf, U. Flörke, Z.Y.D. Espinoza, M.F. Erben, H. Pérez, *J. Mol. Struct.*, 2016, **1111**, 76-83.
42. (a) A. Bauzá, T.J. Mooibroek, A. Frontera, *Chem. Rec*. 2016, **16**, 473-487; (b) A. Frontera, *C*, 2020, **6**, 60; (c) A. Daolio, P. Scilabra, G. Terraneo, G. Resnati, *Coord. Chem. Rev.* 2020, **413**, 213265.
43. (a) S.K. Seth, *Acta Cryst*. 2018, **E74**, 600-606; (b) A. Di Santo, H. Pérez, G.A. Echeverría, O.E. Piro, R.A. Iglesias, R.E. Carbonio, A. Ben Altabef, D.M. Gil, *RSC Adv*. 2018, **8**, 23891-23902; (c) M. Rocha, M.C. Ruiz, G.A. Echeverría, O.E. Piro, A.L. Di Virgilio, I.E. León, A. Frontera, D.G. Gil, *New J. Chem*. 2019, **43**, 18832-18842; (d) M. Madni, M.N. Ahmed, M. Hafeez, M. Ashfaq, M.N. Tahir, D.M. Gil, B. Galmés, S. Hameed, A. Frontera, *New J. Chem*. 2020, **44**, 14592-14603.
44. (a) M.A. Spackman, P.G. Byron, *Chem. Phys. Lett*. 1997, **267**, 215-220; (b) J.J. McKinnon, A.S. Mitchel, M.A. Spackman, *Chem.-Eur. J.* 1998, **4**, 2136-2141; (c) J.J. McKinnon, A.S. Mitchel, M.A. Spackman, *Chem. Commun*. 1998, 2071.
45. C. Jelsh, S. Soudani, C.B. Nash, *IUCrJ*, 2015, **2**, 327-340.

46. A. Saeed, M. Bolte, M.F. Erben, H. Pérez, *CrystEngComm*, 2015, **17**, 7551-7563.
47. C.F. Mackenzie, P.R. Spackman, D. Jayatilaka, M.A. Spackman, *IUCrJ*, 2017, **4**, 575-587.
48. A. J. Edwards, C. F. Mackenzie, P. R. Spackman, D. Jayatilaka, M. A. Spackman, *Faraday Discuss.* 2017, **203**, 93–112.
49. (a)R. Shukla, P. Bandopadhyay, M. Sathe, D. Chopra, *J. Chem. Sci.* 2020, **132**, 19; (b) A. Saeed, Z. Ashraf, H. Nadeem, J. Simpson, H. Pérez, M.F. Erben, *J. Mol. Struct.* **1195**, 796-806.
50. D.M. Gil, H. Pérez, G.A. Echeverría, O.E. Piro, A. Frontera, *ChemistrySelect*, 2020, **5**, 6331-6338.
51. A. Bauzá, S. K. Seth and A. Frontera, *J. Comput Chem*., 2019, **39**, 458-463.
52. C. Garau, A. Frontera, D. Quiñonero, P. Ballester, A. Costa and P. M. Deyà, *ChemPhysChem*, 2003, **4**, 1344-1348.
53. J. Contreras-García, W. Yang and E. R. Johnson, *J. Phys. Chem. A*, 2011, **115**, 12983–12990.
54. (a) M. Maiti, S. Thakurta, G. Pilet, A. Bauza and A. Frontera, *J. Mol. Struct*. 2021, **1226**, 129346; (b) G. Mahmoudi, E. Zangrando, A. Frontera and D. A. Safin, *J. Mol. Struc*t. 2021, **1225**, 129269; (c) G. Mahmoudi, M. Abedi, S. E. Lawrence, E. Zangrando, M. G. Babashkina, A. Klein, A. Frontera and D. A. Safin, *Molecules* 2020, **25**, 4056; (d) G. Mahmoudi, F.A. Afkhami, E. Zangrando, W. Kaminsky, A. Frontera and D. A. Safin, *J. Mol. Struct*. 2021, **1224**, 129188; (e) A. Das, P. Sharma, A. Frontera, A.K. Verma, M. Barcelo-Oliver, S. Hussain and M. K. Bhattacharyya, *J. Mol. Struct*. 2021, **1223**, 129246; (f) G. Mahmoudi, M. Kubicki, D. Choquesillo-Lazarte, B. Miroslaw, E. V. Alexandrov, P. N. Zolotarev, A. Frontera, D. A. Safin, *Polyhedron* 2020, **190**, 114776; (g) L. E. Zelenkov, D. M. Ivanov, E. K. Sadykov, N. A. Bokach, B. Galmes, A. Frontera, V. Yu. Kukushkin, *Cryst. Growth Des*. 2020, **20**, 6956-6965; (h) L. Bofill, R. Prohens, R. Barbas, A. Frontera, *Cryst. Growth Des*., 2020, **20**, 6691-6698; (i) A. V. Kletskov, A. D. Zatykina, M. V. Grudova, A. A. Sinelshchikova, M. S. Grigoriev, V. P. Zaytsev, D. M. Gil, R. A. Novikov, F. I. Zubkov, A. Frontera, *Org. Biomol. Chem*. 2020, DOI:10.1039/d0ob01201g; (j) G. Mahmoudi, S. K. Seth, A. Bauza, F. I. Zubkov, A. Frontera, *Crystals* 2020, **10**, 568; (k) P. K. Bhaumik, A. Banerjee, T. Dutta, S. Chatterjee, A. Frontera, S. Chattopadhyay, *CrystEngComm* 2020, **22**, 5263; (l) T. Basak, A. Frontera, S. Chattopadhyay, *CrystEngComm* 2020, **22**, 5731-5742; (m) J. J. Roeleveld, S. J. Lekanne Deprez, A. Verhoofstad, A. Frontera, J. I. van der Vlugt, T. J. Mooibroek, *Chem.*

Eur. J. 2020, **26**, 10126-10132; (n) A. Bauza, I. Alkorta, J. Elguero, T. J. Mooibroek, A. Frontera, *Angew. Chem. Int. Ed*. 2020, **59**, 17482-17487; (o) N. S. Soldatova, P. S. Postnikov, V. V. Suslonov, T. Yu. Kissler, D. M. Ivanov, M. S. Yusubov, B. Galmes, A. Frontera, V. Yu. Kukushkin, *Org. Chem. Front*. 2020, **7**, 2230-2242.

55. (a) M. V. Vener, A. N. Egorova, A. V. Churakov and V. G. Tsirelson, *J. Comput. Chem*. 2012, **33**, 2303–2309; (b) E. Espinosa , E. Molins and C. Lecomte , *Chem. Phys. Lett*., 1998, **285** , 170–173; (c) A. Bauzá and A. Frontera, *ChemPhysChem*, 2020, **21**, 26-31

View Article Online
DOI: 10.1039/D0NJ03958F

Table of contents entry

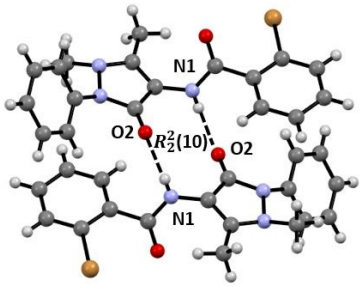

Based on experimental and computational data, a complex network of intermolecular interactions has been rationalized for antipyrine compounds